



Investigation of Aerodynamic Characteristics and Stability of Oblique Wing Airplanes

AUTHOR

Mohammad Zandsalimy

December 9, 2021

Abstract

Oblique wing airplanes were investigated for a long time with the promise of combining efficient subsonic as well as supersonic flight characteristics. The first known oblique wing design was the Blohm & Voss P.202, proposed by Richard Vogt in 1942. Further, NASA AD-1 (Ames-Dryden-1) aircraft utilized a wing that could be pivoted obliquely from zero to 60 degrees during flight. The aircraft was flown 79 times during the research program, which evaluated the basic pivot-wing concept and gathered information on handling qualities and aerodynamics at various speeds and degrees of pivot. Further, there has been several test flights to prove the feasibility and performance of oblique wings. NASA Ames also developed an oblique wing airplane from their F-8 digital-fly-by-wire airplane. This design can produce higher lift to drag ratios over a wide range of flying speeds. Such airplanes, however, show large cross-coupling in their control and dynamic behavior which is not present in conventional symmetrical airplanes. Such behavior must be compensated to obtain acceptable handling qualities. Furthermore, R.T. Jones of NASA Ames Research Center has conducted some of the earliest theoretical studies on this subject, beginning in the 1950s. In the present project, first, I will give a historical review of oblique wing airplanes and other oblique wing studies and summarize the results. I will then use XFLR5 software to analyze the characteristics and performance of NASA AD-1 wing (at zero sweep). I will also utilize lifting line theory to analyze the effect of oblique angle on the induced drag. At low speeds, the most efficient lifting surface is a high aspect ratio elliptically loaded wing because drag due to lift is inversely proportional to the aspect ratio. At transonic and supersonic speeds, however, wave drag is the dominant part of the total drag. A significant advantage of oblique wing arrangements for supersonic flight is that they distribute the lift over about twice the wing length compared to a conventional, symmetrically swept wing. This reduces lift dependent wave drag by a factor of 4 and volume dependent wave drag by a factor of 16.

Keywords: Oblique Wing, Aerodynamic Performance, Airplane Stability.

Contents

Abstract	i
List of Figures	iii
List of Tables	iv
Nomenclature	v
1 Introduction	1
2 AD-1 Aircraft	10
3 XFLR5 Analysis	13
4 Lifting Line Theory Analysis	16
5 Far Field Analysis and the Trefftz Plane	26
5.1 Nonplanar Wakes	28
5.2 Munk's Stagger Theorem	28
6 Conclusion	29
References	30



List of Figures

1	A Grumman F-14 Tomcat during a test of an unusual asymmetric wing configuration	2
2	Comparison of load and moment distribution for oblique and symmetrically swept wings	3
3	Robert T. Jones making a violin	4
4	The AD-1 oblique wing research aircraft	5
5	Comparison of length of oblique and symmetrically swept wings	6
6	Five different configurations of wings flying at Mach=0.9	7
7	Comparison of drag components of different wing configurations flying at Mach=0.9	7
8	Prediction of drag coefficient vs. Mach number	8
9	Oblique all wing concept proposed by G. H. Lee	9
10	An oblique all wing aircraft model	9
11	Mach line in two different angles of sweep	10
12	AD-1 aircraft at flight	11
13	Three view sketch of Ad-1 aircraft	12
14	Lift coefficient vs. angle of attack at $U_{\infty} = 80$ m/s	13
15	Drag coefficient vs. angle of attack at $U_{\infty} = 80$ m/s	14
16	Lift coefficient vs. drag coefficient at $U_{\infty} = 80$ m/s	14
17	C_L/C_D vs. angle of attack at $U_{\infty} = 80$ m/s	15
18	Lift coefficient distribution over half span at $\alpha = 2$ degrees and $U_{\infty} = 80$ m/s	15
19	Induced angle of attack distribution over half span at $\alpha = 2$ degrees and $U_{\infty} = 80$ m/s	16
20	Replacement of the finite wing with a bound vortex	17
21	Downwash distribution over half span of a wing with constant circulation	17
22	The induced velocity dV at P by an element of the vortex filament of strength Γ	18
23	Top view of an oblique horseshoe vortex	19
24	Downwash distribution over the span of an oblique wing with constant circulation	20
25	Superposition of a finite number of horseshoe vortices along the lifting line	21
26	Top view of many oblique horseshoe vortices making a finite wing	21
27	Downwash distribution along the span of an elliptic oblique wing	23
28	Nondimensionalized Induced drag distribution along the span of an elliptic oblique wing at $U_{\infty} = 300$	24
29	Nondimensionalized Induced drag distribution along the span of an elliptic oblique wing at $U_{\infty} = 100$	25
30	control volume around a finite wing	26

List of Tables

1	AD-1 aircraft characteristics	11
2	AD-1 wing geometry	12
3	Total nondimensionalized induced drag vs. oblique angle of sweep at $U_{\infty} = 300$	25
4	Total nondimensionalized induced drag vs. oblique angle of sweep at $U_{\infty} = 100$	25



Nomenclature

α	Angle of Attack
α_i	Induced Angle of Attack
\mathcal{R}	Aspect Ratio
Γ	Vortex Circulation
Λ	Sweep Angle
ρ	Fluid Density
b	Wing Span
C	Speed of Sound
C_D	Drag Coefficient
C_L	Lift Coefficient
D	Drag Force
D_i	Induced Drag
L	Lift Force
P	Pressure
P_∞	Freestream Pressure
S	Area
U	Flow Velocity
u	Velocity in x Direction
U_∞	Freestream Velocity
v	Velocity in y Direction
w	Velocity in z Direction
$w(y)$	Downwash
Y	Side Force
IC_d	Induced Drag
PC_d	Parasite Drag
TC_d	Total Drag



1 Introduction

No doubt, straight wing airplanes are most efficient in low speed flight, but swept wings are essential in an aircraft designed for transonic or supersonic flight. Supersonic flight missions usually have high swept (or even delta) wings. Unfortunately, the stall speed increases with increasing sweep which means longer takeoff distance requirement. Further, high sweep can increase the parasite drag in subsonic flights which increases the fuel consumption in this phase. A variable sweep wing allows the use of optimum sweep angle for the aircraft's current phase of flight (related to flight speed). A number of experimental designs were carried out prior to the 1970s and a few variable sweep airplanes (including Grumman F-14 Tomcat) are still in use. Figure 1 shows the Grumman F-14 Tomcat aircraft testing an unusual asymmetric wing configuration with one wing at minimum sweep and the other at maximum sweep. Recent advances in flight control and structural materials allows more advancement in variable geometry aircraft. New designs are less focused on variables sweep to achieve the required performance. Instead, wings are given complicated flaps on both leading and trailing edges that change the effective camber or chord of the wing to adjust to the flight regime. Such configurations are also a form of variable geometry wings [1]. Variable geometry wings are wings that are capable of changing their shape in some way during flight which can be divided into the following categories:

- Variable sweep wings known as swing wing (e.g. Sukhoi Su-24).
- Variable incidence wings with an adjustable angle of incidence relative to its fuselage (e.g. RF-8A Crusader).
- Variable camber (and/or chord) wings in which the leading and/or trailing edge sections of the whole wing pivot to increase the effective camber, modifying the maximum lift coefficient.
- Oblique wings also known as slewed wings which are designed in a way to rotate about the center point, so that one tip is swept forward while the opposite tip is swept aft.



Figure 1: A Grumman F-14 Tomcat during a test of an unusual asymmetric wing configuration (courtesy of San Diego Air & Space Museum Archives).

As the 1940s came to a close, military aircraft manufacturers in the United States faced a disturbing problem. The Bell X-1 had broken the sound barrier, and both the Air Force and the Navy were looking for next generation aircraft that could operate at supersonic speeds. But preliminary tests of models indicated that even the best designs put forth by industry engineers were not going to be able to achieve that goal. A sharp increase in drag at speeds approaching mach number one was proving too much for the limited power of jet engines in that time to overcome. The solution to this frustrating impasse was found by Richard T Whitcomb, a young aerodynamic scientist at NACA Langley Research Center in Hampton, Virginia. His development of the "area rule" revolutionized how engineers looked at high-speed drag and impacted the design of virtually every transonic and supersonic aircraft ever built. In recognition of its far-reaching impact, Whitcomb's area rule was awarded the 1954 Collier Trophy [2].

The Whitcomb area rule is a design technique used to reduce an aircraft's drag at transonic and supersonic speeds. Transonic acceleration is considered an important performance metric for airplanes and which is directly dependent upon wave drag. This rule states that small changes in cross sectional area of the aircraft will prevent high wave drag at transonic flight regimes. Straight wings are a large change in the cross sectional area of the airplane. Swept wings have a more gradual change in the cross sectional area. Further, oblique wings tend to remedy this problem in an unusual and effective way. An oblique wing can vary the wing sweep with a single pivot that is primarily loaded in tension, trading aspect ratio for fineness ratio¹ by sweeping one wing tip forward and the other wing tip back. This design allows a greater reduction in the wave drag, automatically accounts for area ruling, and reduces pivot torque and bending loads as well as fuselage loads. As presented in figure 2, the torque and bending loads from wing pivots can be avoided utilizing an oblique wing.

¹The fineness ratio is the ratio of the length of a body to its maximum width

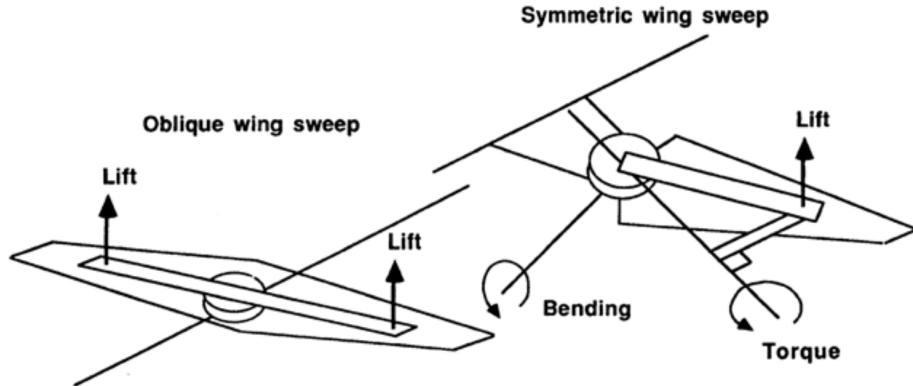


Figure 2: Comparison of load and moment distribution for oblique and symmetrically swept wings (courtesy of NASA Langley Research Center).

Oblique wing airplanes can be utilized for both military and civilian missions. Main advantages of such airplanes is for airplanes with subsonic as well as supersonic regimes in their flight envelope. Oblique wing configuration will have lower wave drag, less structural weight, and reduced hangar parking and storage area compared to other variable geometry aircraft. Many analytical studies, wind tunnel tests, and low speed light weight flights have been conducted on such airplanes, but no high performance aircraft has been developed due to high risks associated with such revolutionary designs [3]. The advantages of oblique wings cannot be obtained without overcoming many design challenges. Dynamic behavior and response of such wing configuration is not even close to the conventional symmetric airplanes. The flight control system has to provide lateral-directional (roll-yaw) decoupling so that good stability and handling are provided for the pilot during the flight envelope.

One of the most notable scientists to work on the development and advancement of oblique wings is American aerodynamicist and aeronautical engineer, Robert Thomas Jones. Between 1946 and 1958, Robert T. Jones conducted various studies on swept and delta-wing aerodynamics, making notable contributions to understanding the relationship between planform choice and aerodynamic performance. Jones was firmly committed to the study of bilaterally symmetric swept-wing shapes. But in 1952, he deviated from the bilaterally symmetric path to address the case of the elliptical wing. The elliptical wing is one of the oldest and most pleasing aerodynamic shapes. Earlier in his career, Jones had studied the conventional elliptical wing, and now, in the early supersonic era, he returned to study it, finding that an elliptical wing set at an oblique angle not only had a highly desirable uniform lift distribution, but a greatly reduced drag as well [4]. Figure 3 shows a photo of R.T. Jones working on a violin. Also in this photo, notice the oblique wing radio controlled model airplane and a reflector telescope, also made by Jones.



Figure 3: Robert T. Jones making a violin (courtesy of Roger Ressmeyer from Corbis Images).

I am sure model aircraft have a long and distinguished history of contributing to the development of aeronautics. Jones made a balsa wood model of an oblique wing airplane which he flew at the first International Congress of the Aeronautical Sciences (ICAS), held in Madrid, Spain, in September 1958. A great deal of work has been done since on oblique wing aircraft including design work by Boeing, General Dynamics, and Lockheed, wind tunnel testing and analysis by NASA, and flight testing of models and piloted aircraft. Figure 4 shows the AD-1 oblique wing research aircraft in flight.



Figure 4: The AD-1 oblique wing research aircraft (courtesy of NASA Photo ECN 13305-4).

The general idea is to design an aircraft that performs with high efficiency as the Mach number changes during flight envelope. Since different types of drag dominate in each flight regime, uniting high performance designs for each regime into a single airframe can be challenging. Induced drag is the dominant part in low Mach number flight, while wave drag becomes important at high Mach numbers. One way to reduce induced drag is to increase the effective wingspan of the lifting surface as seen in most gliders. One important thing about gliders is their low take off weight which suggests very low lift generation which in turn means that structural concerns are very important in glider construction. An ideal wing has infinite span without induced drag. At lower air speeds, an oblique wing is positioned perpendicular to the fuselage (just like a conventional wing) to provide maximum lift and control qualities. As the flight speed increases, the wing is pivoted to increase the oblique angle which reduces drag and fuel consumption.

Further, at higher Mach numbers, wave drag is dominant. Sweeping the wings away from the nose (where shock waves happen) can keep the wings downstream of the wave which greatly reduces drag. By actively increasing sweep as Mach number increases, high efficiency is possible for a wide range of air speeds. Although one of the principal advantages involves reduced supersonic wave drag, the concept has other merits as well.

There are three main components of wave drag as follows:

- Volume distribution (i.e. area rule)

$$D \sim \frac{\text{Volume}^2}{\text{Length}^4} \quad (1)$$

- Lift distribution

$$D \sim \frac{\text{Lift}^2}{\text{Length}^2} \quad (2)$$

- Sweep effect (at root)

$$D \sim \cos(\Lambda) \quad (3)$$

Figure 5 compares the length of an oblique wing and a symmetrically swept wing with the same sweep angle. Length of the oblique wing is almost twice as much as the symmetric swept wing. This means that the wave drag component due to volume distribution is about $\frac{1}{16}$ and the component due to lift distribution is about $\frac{1}{4}$ when comparing the oblique to swept wing. Furthermore, when compared to an aircraft with symmetric variable sweep, the oblique wing has little change in the aerodynamic center position. This keeps the stability at reasonable levels and avoids large trim changes or complex fuel-pumping schemes.

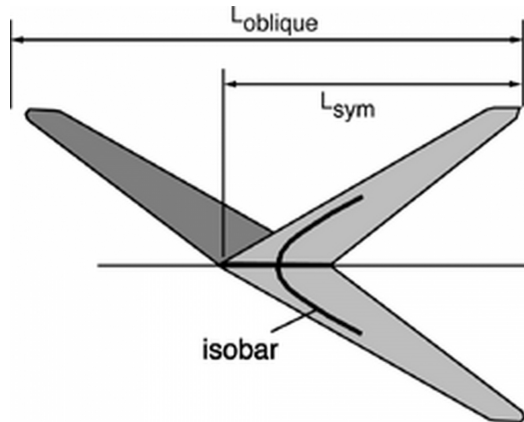


Figure 5: Comparison of length of oblique and symmetrically swept wings (courtesy of Could not Find the Source).

Figure 7 shows a comparison between various drag components of the configurations presented in figure 6 for flight at a Mach number of 0.9. As seen here, the oblique wing at 50° has less total drag than all configurations, with even less wave drag than the delta wing. The viscous drag of the oblique wing is less than the delta wing due to less area. Further, the worst performing wing is the simple configuration without any sweep which sports almost twice as much drag as the oblique wing at 50° . The wave drag has been reduced in all the swept wing planforms but the oblique wing with 30° sweep has 8.95% less total drag compared to sweptback wing of 30° sweep and 40.63% lower total drag compared to 0° sweep. The oblique wing with 50° sweep has 34.8% less total drag compared to sweptback wing of 30° sweep, 10.17% less compared to Delta wing of 65° sweep and 57.49% less compared to 0° sweep. R. T. Jones predicted such benefits before experimental testings. Figure 8 shows his prediction of drag coefficients vs. Mach number for a symmetrically swept wing and an oblique wing at 50° .

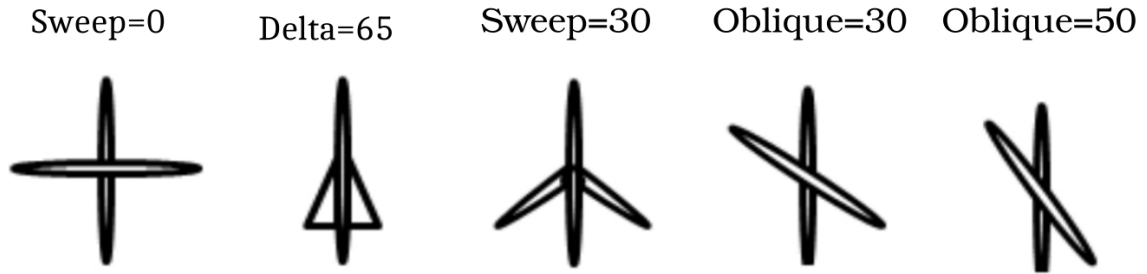


Figure 6: Five different configurations of wings flying at $\text{Mach} = 0.9$ [5].

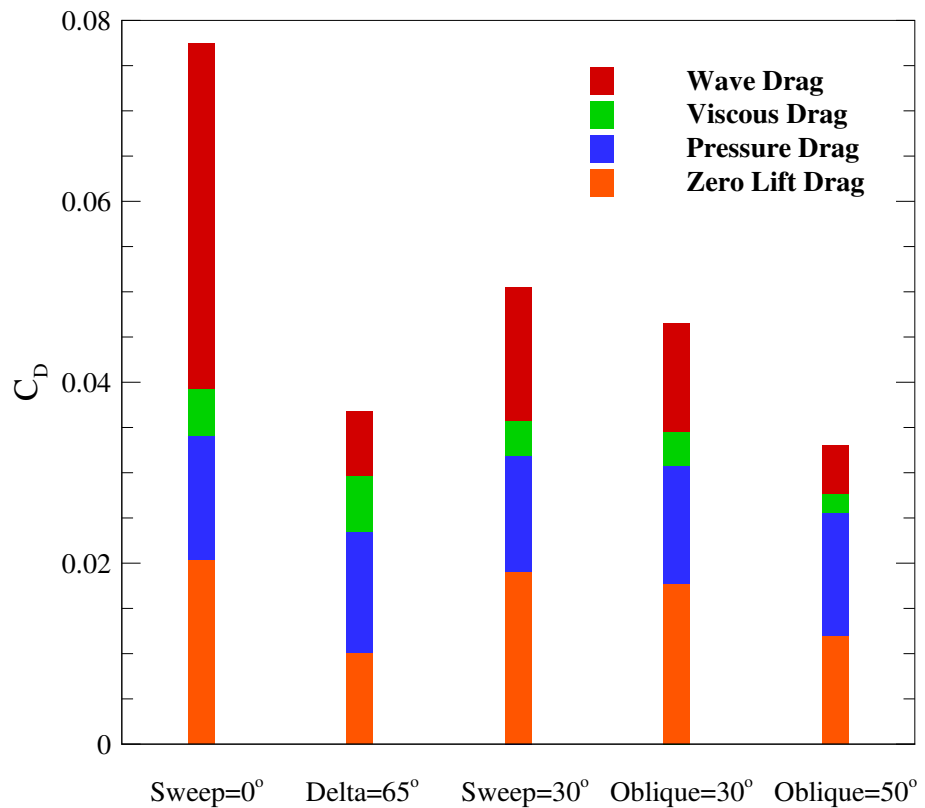


Figure 7: Comparison of drag components of different wing configurations flying at $\text{Mach} = 0.9$ [5].

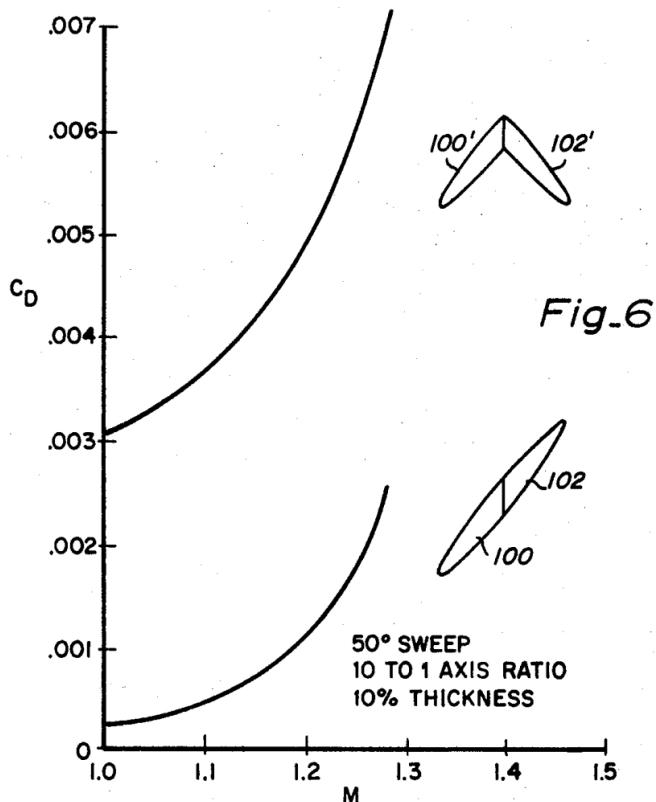


Figure 8: Prediction of drag coefficient vs. Mach number [6].

The concept of an oblique all wing aircraft was first proposed by Lee [7] in the early 1960's, but subsequent research on oblique wing aircraft up to the mid 1980's concerned oblique wing/body aircraft with the oblique wing pivoted from a conventional fuselage. The 3-view sketch of figure 9 shows the concept proposed by Lee. Despite several questions about stability and control, this concept can be made to fly. The model shown in figure 10 weighed about 80 lb (36 kg) with a 20 ft (6 m) wing span and was powered by two ducted fan engines. The aircraft is unstable and controlled actively with a custom built flight control computer. The project was undertaken at Stanford University in 1991-1994, principally by Steve Morris and Ben Tigner [8].

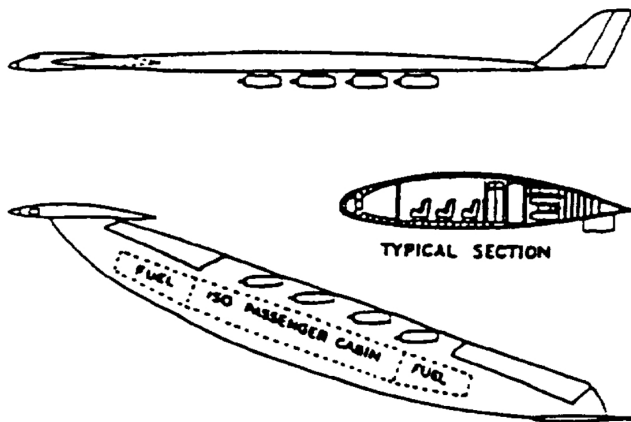


Figure 9: Oblique all wing concept proposed by G. H. Lee [7].



Figure 10: An oblique all wing aircraft model [8].

One of R. T. Jones explanations on the reduced wave drag was about pressure signals (Mach lines) and shock waves. Elementary pressure signals propagate at the speed of sound relative to a fluid. In a subsonic oncoming stream, the disturbance from an unswept wing (or any obstacle for that matter) propagates upstream against the flow and causes the streamlines to begin to curve to avoid the obstacle, thus keeping the drag to a desirably low value. In a supersonic flight, by contrast, signals are confined to a shock wave originating at a point of disturbance. Jones considers an infinitely long wing immersed in a supersonic flow of speed V and swept at different angles in relation to a Mach line. For angles of sweep β less than

that of the Mach line (Figure 11a), the leading edge cannot affect the approaching flow, which thus impacts the airfoil undisturbed, resulting in a large drag. For angles of sweep greater than that of the Mach line (Figure 11b), the wing experiences a subsonic flow. As a result, the streamlines will curve around and follow paths appropriate to a subsonic flow and the drag can be expected to be correspondingly low [9].

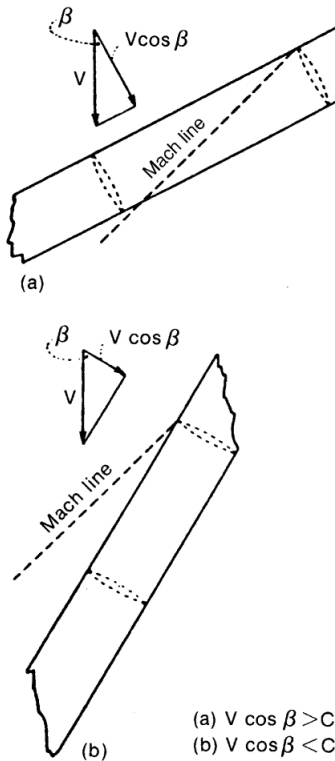


Figure 11: Mach line in two different angles of sweep [10].

2 AD-1 Aircraft

The AD-1 airplane consists of a high fineness ratio fuselage with two French Microturbo TRS-18 engines, each with a sea level thrust rating of 220 pounds. The engines are mounted on short aft pylons on the side of the fuselage and consume 72 gallons of jet fuel stored in two fuselage tanks installed fore and aft of the wing pivot. The AD-1 has conventional horizontal and vertical tails, fixed gear, and a high aspect ratio ($A = 11.3$ zero sweep) oblique wing. The wing can be pivoted in flight from a 0 degree to 60 degree sweep (with the right wing forward) on a pivot point at the 40% of root chord location. The center of gravity while in flight was generally within a few percent of the nominal quarter root chord position. Table 1 summarizes the general and performance characteristics of AD-1 aircraft. Figure 12 shows the overhead view of this aircraft in a flight with non zero oblique angle. Figure 13 shows three view sketch of AD-1 aircraft. Using this photo and the specifications provided in table 1, the wing geometry is extracted to be used latter on. This wing model has zero angle of

incidence and dihedral. This geometry is presented in table 2. Another important note is that this aircraft does not utilize flaps.

Table 1: AD-1 aircraft characteristics.

Crew	1 (pilot)
Length	38 ft 10 in (11.83 m)
Wingspan	32 ft 4 in (9.85 m) unswept
Lower wingspan	16 ft 2 in (4.93 m) swept 60° sweep angle
Height	6 ft 9 in (2.06 m)
Wing area	93 sq ft (8.6 m ²)
Airfoil	NACA 3612-02, 40
Empty weight	1450 lb (658 kg)
Gross weight	2145 lb (973 kg)
Fuel capacity	80 US gallons (300 l)
Powerplant	2× microturbo TRS 18 turbojets, 220 lbf (0.98 kN) thrust each
Maximum speed	200 mph (320 km/h, 170 kn)
Service ceiling	12000 ft (3700 m)



Figure 12: AD-1 aircraft at flight (courtesy of NASA Photo ECN 15846).

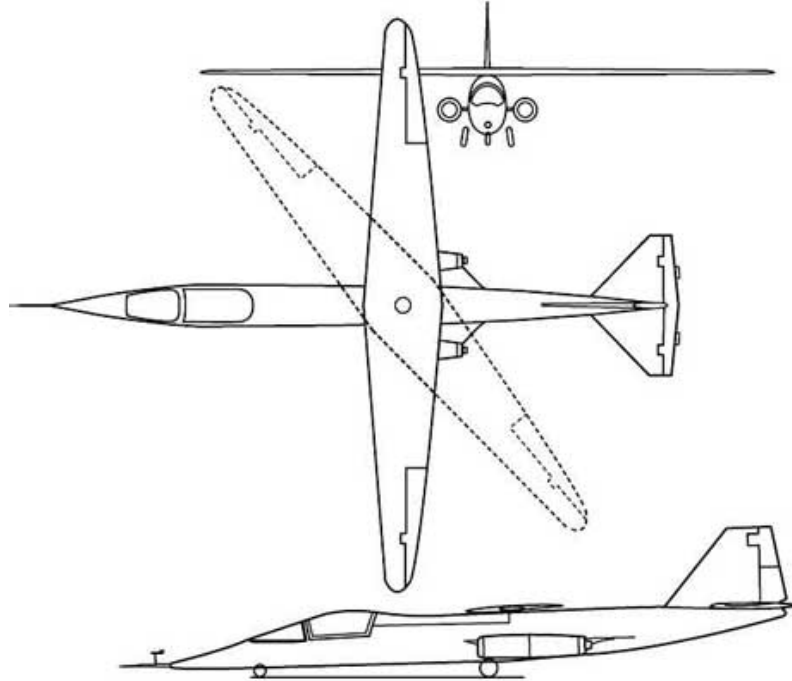


Figure 13: Three view sketch of Ad-1 aircraft (courtesy of NASA Dryden AD-1 Graphics Collection).

Table 2: AD-1 wing geometry.

y	chord	offset
0	1.338	0
0.965	1.185	0.071
2.7	0.87	0.224
3.578	0.717	0.28
3.991	0.621	0.315
4.357	0.544	0.341
4.775	0.382	0.392
4.925	0	0.575

Structurally, the airplane consists of a fiberglass reinforced plastic sandwich with a core of rigid foam. The thickness varies from 17 plies at the wing root to 4 plies at the tip. Except for the wing pivot, all other components were designed to a 6 g load limit capacity. The wing pivot was designed to withstand ± 25.0 g loading. The airplane weighs approximately 2100 pounds and has potential performance speeds up to 175 knots and flight at altitudes of up to 15000 feet. The above specifications were considered conservative since the aircraft was not expected to exceed 5 g loading or 150 knot speed in order to accomplish the program's research goals [11].

3 XFLR5 Analysis

In this section, the wing of AD-1 aircraft is imported into XFLR5 software and analyzed in different conditions. Unfortunately, XFLR5 is not able to analyze oblique wings. As a result, this study will be carried out for the wing at zero degrees of oblique angle. First test is done at a constant speed of 80 m/s and at a cruise height of 3000 m. In this conditions, tip Reynolds number is about 2 million, while root Reynolds number is about 7 million. Figure 14 shows the plot of lift coefficient vs. angle of attack. The lift coefficient slope is about 0.092726 per degree and stall occurs at 21 degrees. Zero lift angle is -1.5546 degrees. Different components of drag and total drag are plotted vs. angle of attack in figure 15. At high angles of attack (near stall) the rate of increment in induced drag reduces slightly and the rate of increment in parasite drag increases. Further, figure 16 shows the drag polar of this wing. The minimum drag coefficient happens at -0.5 degrees angle of attack which corresponds to a drag coefficient of 0.004618 and a lift coefficient of 0.100232. Figure 17 shows the plot of C_L/C_D vs. angle of attack. The maximum value of C_L/C_D happens at $\alpha = 2$ degrees and corresponds to a value of $C_L/C_D = 43.3543$. At the design angle of attack the distribution of lift coefficient and induced angle of attack over the span of the wing are plotted in figures 18 and 19, respectively. As seen in figure 18, lift coefficient increases up to about 50% of half span and the stays almost constant up to 90% and then suddenly decreases. The same thing in reverse happens to induced angle of attack. As seen in figure 19, induced angle of attack decreases until about 50% of half span and the stays almost constant up to 90% and then suddenly increases.

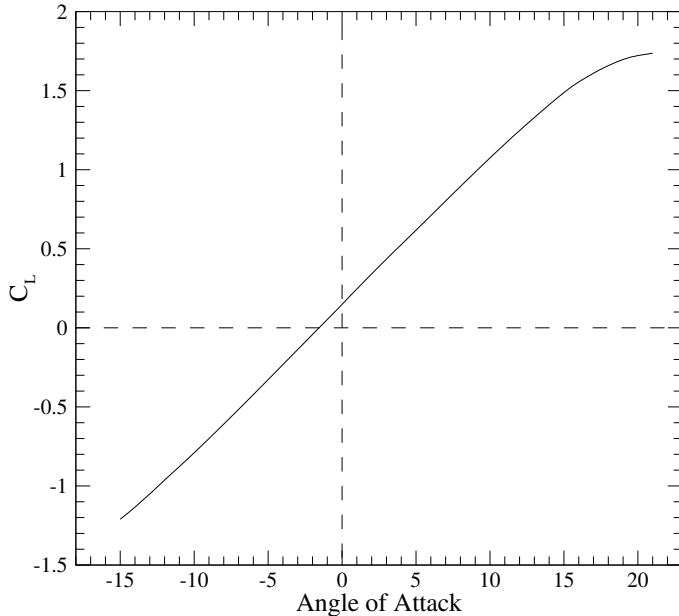
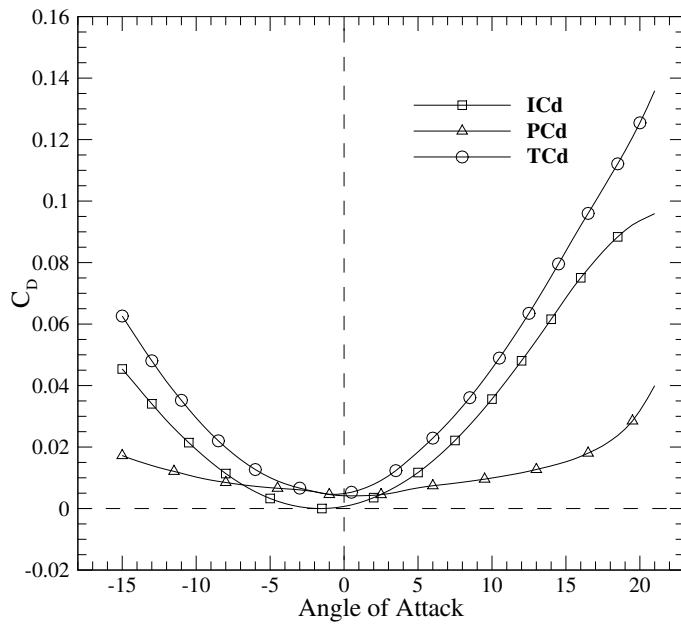
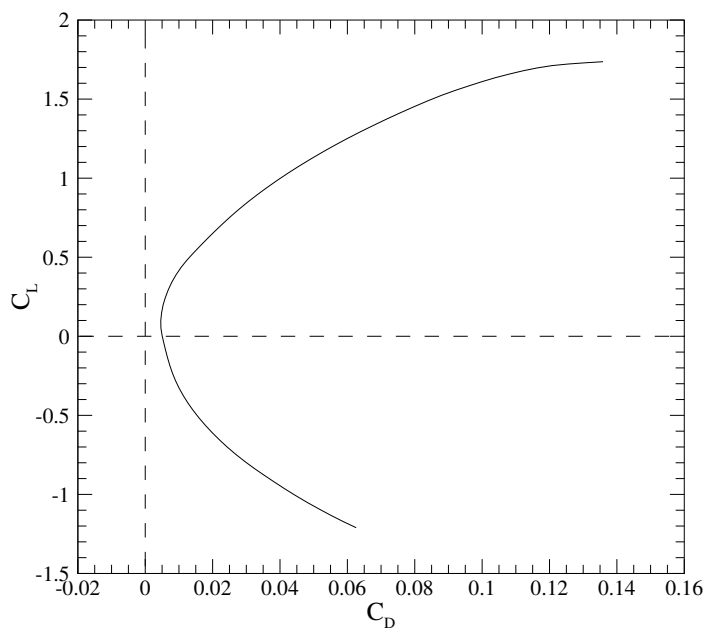
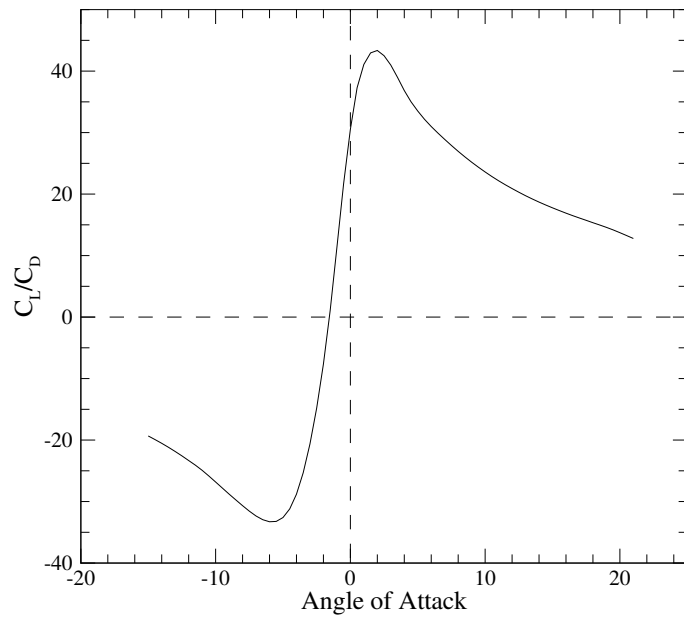
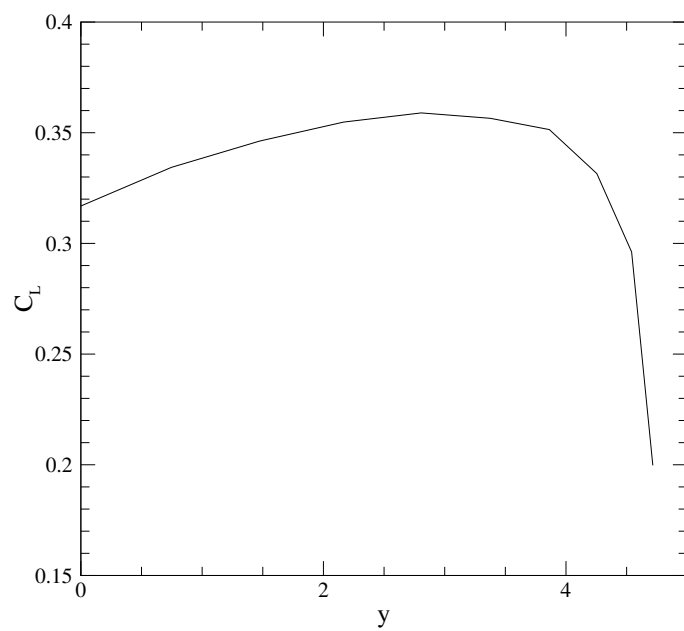


Figure 14: Lift coefficient vs. angle of attack at $U_\infty = 80$ m/s.

Figure 15: Drag coefficient vs. angle of attack at $U_{\infty} = 80$ m/s.Figure 16: Lift coefficient vs. drag coefficient at $U_{\infty} = 80$ m/s.

Figure 17: C_L/C_D vs. angle of attack at $U_\infty = 80$ m/s.Figure 18: Lift coefficient distribution over half span at $\alpha = 2$ degrees and $U_\infty = 80$ m/s.

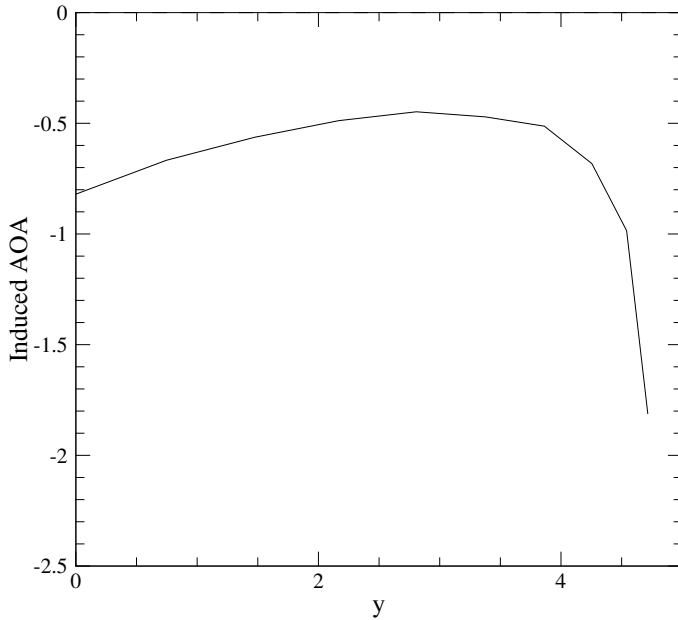


Figure 19: Induced angle of attack distribution over half span at $\alpha = 2$ degrees and $U_\infty = 80$ m/s.

4 Lifting Line Theory Analysis

From the Kutta-Joukowski theorem, a bound vortex of strength Γ (a vortex filament which is somehow bound to a fixed location in the flow) will experience a force $L = \rho U \Gamma$. In which U and ρ are free stream velocity and density, respectively. We can replace a finite wing of span b with a bound vortex, extending from $y = -b/2$ to $y = b/2$. However, according to Helmholtz's theorem, a vortex filament cannot end in the fluid and has to continue to infinity or just end in a wall. As a result assume that the vortex filament continues downstream to infinity as two free vortices from wing tips. This setup is presented in figure 20 which is similar to a horseshoe and is called a horseshoe vortex. Now consider the downwash w induced by the two trailing vortices along the span. Both of these vortices induce a velocity pointing downward. The induced downwash can be described as equation 4. The distribution of downwash along the span of a wing with constant circulation of $\Gamma = 4\pi$ (horizontal axis is nondimensionalized with $b/2$) is presented in figure 21. Notice that downwash goes to negative infinity at the tips.

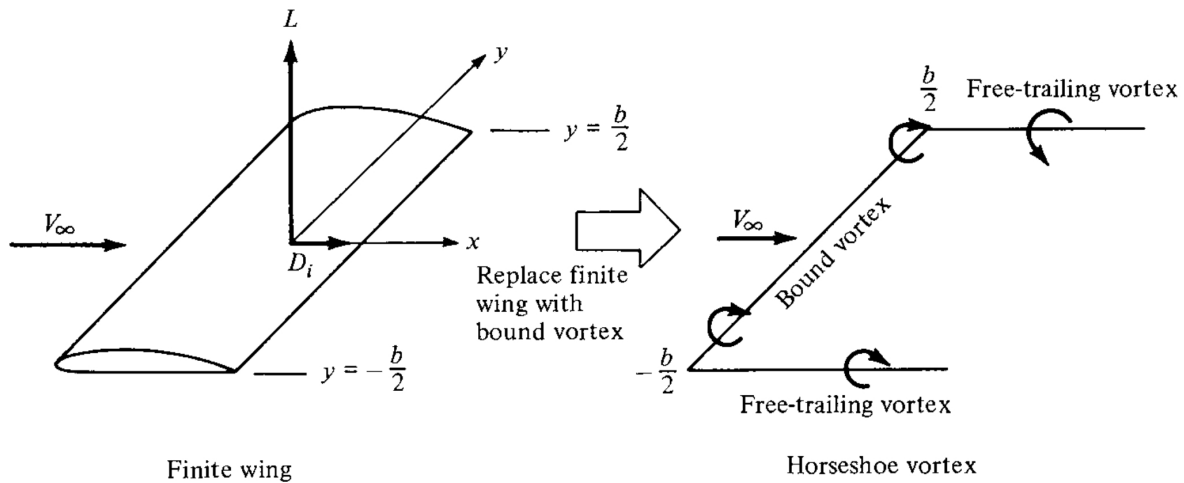


Figure 20: Replacement of the finite wing with a bound vortex [12].

$$w(y) = -\frac{\Gamma}{4\pi} \frac{b}{\left(\frac{b}{2}\right)^2 - y^2} \quad (4)$$

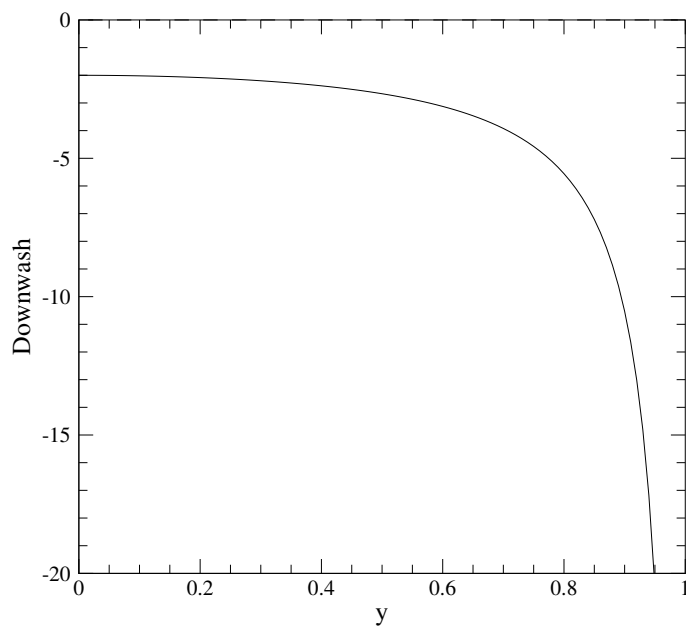


Figure 21: Downwash distribution over half span of a wing with constant circulation.

Assume a vortex filament of strength Γ is present in the space as in figure 22. An element of this vortex filament will induce a velocity dV at point P which can be presented as in

equation 5 according to Biot-Savart law. Now imagine a finite straight piece of a bound vortex whom ends make angles θ_1 and θ_2 with point P. In such conditions, the induced velocity at point P will be as in equation 6.

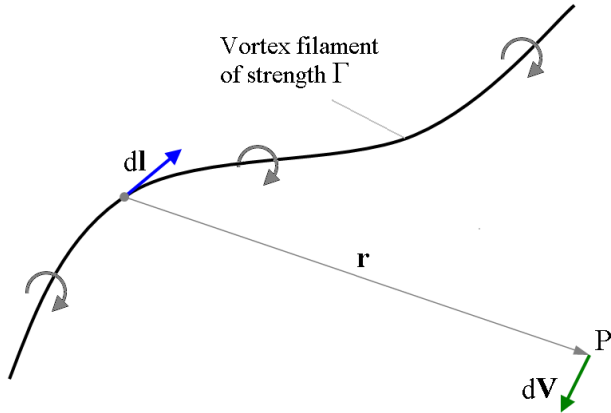


Figure 22: The induced velocity dV at P by an element of the vortex filament of strength Γ .

$$d\vec{V} = \frac{\Gamma}{4\pi} \frac{d\vec{l} \times \vec{r}}{|r^3|} \quad (5)$$

$$V = -\frac{\Gamma}{4\pi r} (\cos(\theta_1) + \cos(\theta_2)) \quad (6)$$

Now assume we have replaced an oblique wing at a sweep angle of Λ with a single horseshoe vortex as in figure 23. The induced velocity on any y on the span of the wing can be calculated as in equation 7. This equation can be rewritten in form of equation 8. The distribution of downwash along the span of an oblique wing at different sweep angles of 0, 30, 45, and 60 degrees, with constant circulation of $\Gamma = 4\pi$ (horizontal axis is nondimensionalized with $b/2$) is presented in figure 24. As seen in this figure, downwash at tips goes to infinity again. This time however, we don't have a symmetric distribution of downwash along the span. For an oblique wing with non zero sweep, downwash increases on the right half span (swept forward). However, downwash is less than the normal wing on the outer part of the left half of the wing (swept back).

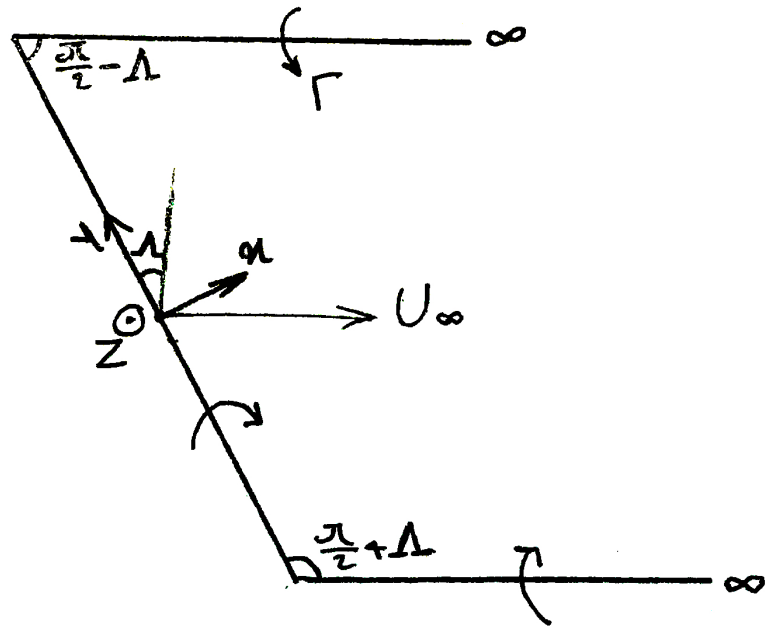


Figure 23: Top view of an oblique horseshoe vortex.

$$w(y) = -\frac{\Gamma}{4\pi(\frac{b}{2} + y)\cos(\Lambda)} \left(\cos\left(\frac{\pi}{2} + \Lambda\right) + \cos(0) \right) - \frac{\Gamma}{4\pi(\frac{b}{2} - y)\cos(\Lambda)} \left(\cos\left(\frac{\pi}{2} - \Lambda\right) + \cos(0) \right) \quad (7)$$

$$w(y) = -\frac{\Gamma}{4\pi \cos(\Lambda)} \left(\frac{2y \sin(\Lambda) + b}{\left(\frac{b}{2}\right)^2 - y^2} \right) \quad (8)$$

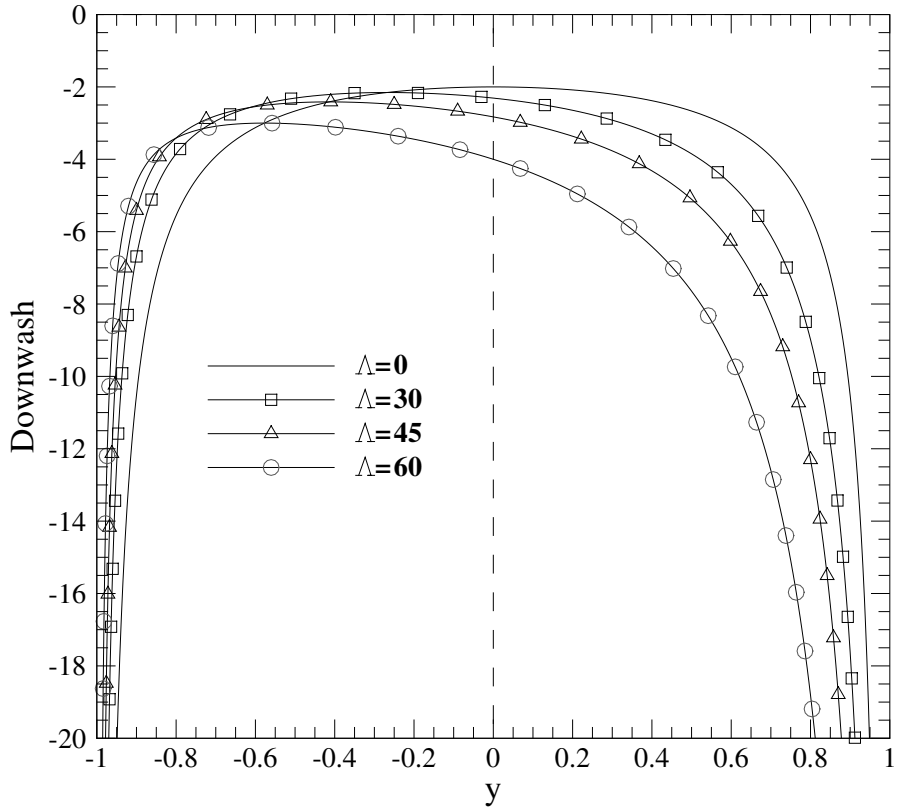


Figure 24: Downwash distribution over the span of an oblique wing with constant circulation.

Downwash distribution due to a single horseshoe vortex does not simulate a finite wing very well. Especially, downwash going to infinity at the tips cannot be very realistic. Prandtl found a remedy for this issue and that was to use a large number of horseshoe vortices to simulate the effect more thoroughly. This concept is shown in figure 25 with only 3 horseshoe vortices. Derivation procedure of a traditional wing is presented in detail in [12] and we are not going to repeat that here. Instead, I will be deriving similar equations, only for an oblique wing at a Λ angle.

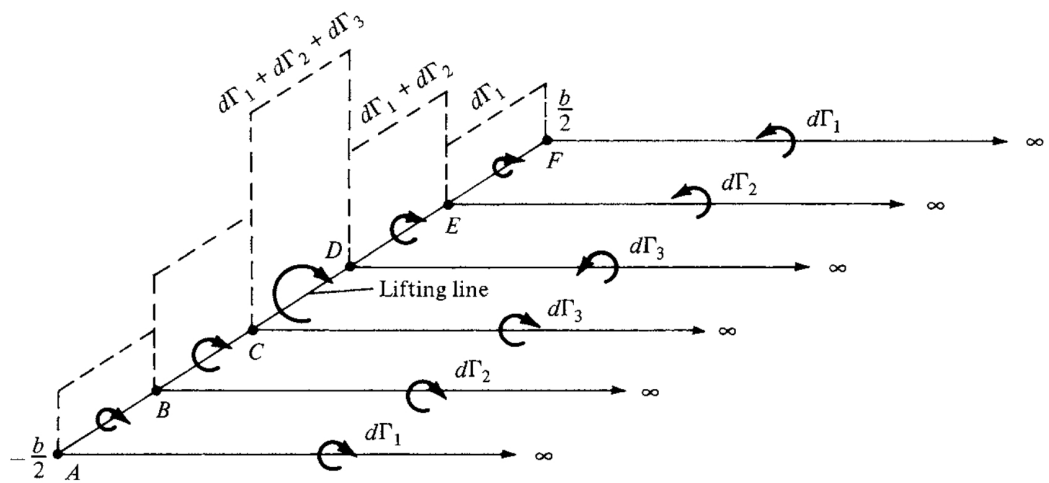


Figure 25: Superposition of a finite number of horseshoe vortices along the lifting line [12].

Assume that we simulate the effect of a finite wing with an infinite number of oblique horseshoe vortices as in figure 26. The induced velocity at point y_o on the lifting line from a vortex element $d\Gamma = (d\Gamma/dy)dy$ at position y can be expressed as equation 9. A simpler version of this equation is presented in equation 10. Now we have to integrate this equation over the span of the wing as in equation 11. The induced angle of attack is described as the negative ratio of downwash to freestream velocity which is presented in equation 12.

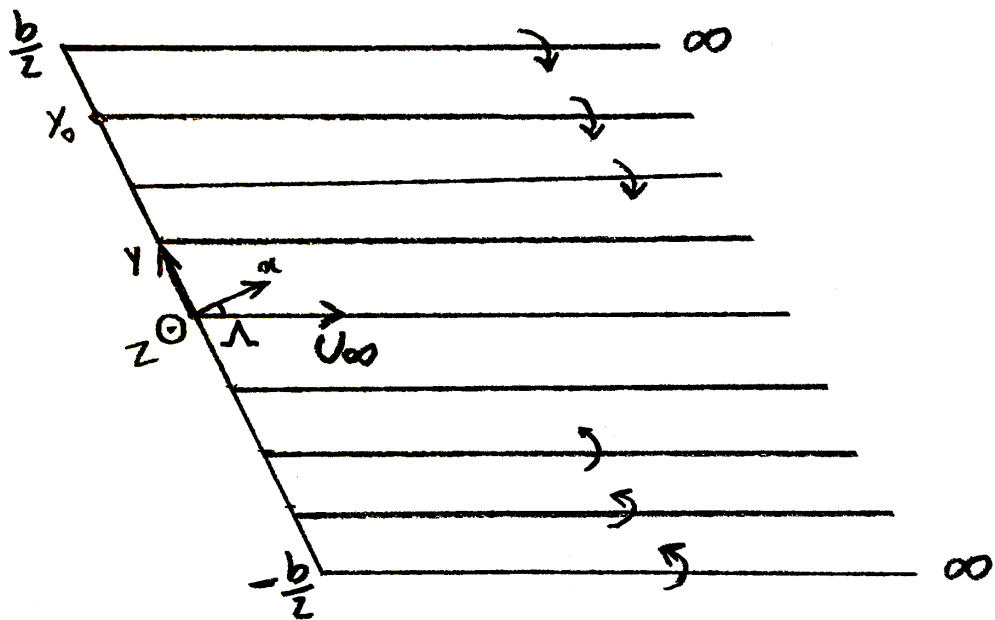


Figure 26: Top view of many oblique horseshoe vortices making a finite wing.

$$dw = -\frac{(d\Gamma/dy)dy}{4\pi(y_o - y)\cos(\Lambda)} \left(\cos\left(\frac{\pi}{2} + \text{sign}(y_o - y)\Lambda\right) + \cos(0) \right) \quad (9)$$

$$dw = -\frac{(d\Gamma/dy)dy}{4\pi(y_o - y)\cos(\Lambda)} (-\sin(\text{sign}(y_o - y)\Lambda) + 1) \quad (10)$$

$$w(y_o) = -\frac{1}{4\pi} \int_{-b/2}^{b/2} \frac{(-\sin(\text{sign}(y_o - y)\Lambda) + 1)(d\Gamma/dy)dy}{(y_o - y)\cos(\Lambda)} \quad (11)$$

$$\alpha_i(y_o) = \frac{1}{4\pi U_\infty} \int_{-b/2}^{b/2} \frac{(-\sin(\text{sign}(y_o - y)\Lambda) + 1)(d\Gamma/dy)dy}{(y_o - y)\cos(\Lambda)} \quad (12)$$

Let's use a variable change as $y = \frac{b}{2} \cos(\theta)$ and $y_o = \frac{b}{2} \cos(\theta_o)$ and rewrite equation 11 as follows.

$$w(\theta_o) = \frac{1}{4\pi} \int_{\pi}^0 \frac{(-\sin(\text{sign}(\theta_o - \theta)\Lambda) + 1)(d\Gamma/dy)\sin(\theta)d\theta}{(\cos(\theta_o) - \cos(\theta))\cos(\Lambda)} \quad (13)$$

$$w(\theta_o) = \frac{1}{4\pi} \int_0^\pi \frac{(-\sin(\text{sign}(\theta_o - \theta)\Lambda) + 1)(d\Gamma/dy)\sin(\theta)d\theta}{(\cos(\theta) - \cos(\theta_o))\cos(\Lambda)} \quad (14)$$

$d\Gamma/dy$ can be rewritten in the following form.

$$\frac{d\Gamma}{dy} = \frac{d\Gamma}{d\theta} \frac{d\theta}{dy} = -\frac{d\Gamma}{d\theta} \frac{1}{\frac{b}{2}\sin(\theta)} \quad (15)$$

As a result, equation 14 can be changed as follows.

$$w(\theta_o) = -\frac{1}{2\pi b} \int_0^\pi \frac{(-\sin(\text{sign}(\theta_o - \theta)\Lambda) + 1)(d\Gamma/d\theta)d\theta}{(\cos(\theta) - \cos(\theta_o))\cos(\Lambda)} \quad (16)$$

$$w(\theta_o) = -\frac{1}{2\pi b \cos(\Lambda)} \int_0^\pi \frac{(-\sin(\text{sign}(\theta_o - \theta)\Lambda) + 1)(d\Gamma/d\theta)d\theta}{(\cos(\theta) - \cos(\theta_o))} \quad (17)$$

$$w(\theta_o) = -\frac{1}{2\pi b \cos(\Lambda)} \left[\int_0^\pi \frac{(d\Gamma/d\theta)d\theta}{(\cos(\theta) - \cos(\theta_o))} - \int_0^\pi \frac{\sin(\text{sign}(\theta_o - \theta)\Lambda)(d\Gamma/d\theta)d\theta}{(\cos(\theta) - \cos(\theta_o))} \right] \quad (18)$$

$$w(\theta_o) = -\frac{1}{2\pi b \cos(\Lambda)} \left[\int_0^\pi \frac{(d\Gamma/d\theta)d\theta}{(\cos(\theta) - \cos(\theta_o))} - \sin(\Lambda) \int_0^{\theta_o} \frac{(d\Gamma/d\theta)d\theta}{(\cos(\theta) - \cos(\theta_o))} \right. \\ \left. + \sin(\Lambda) \int_{\theta_o}^\pi \frac{(d\Gamma/d\theta)d\theta}{(\cos(\theta) - \cos(\theta_o))} \right] \quad (19)$$

For an elliptical circulation distribution of $\Gamma = \Gamma_o \sin(\theta)$ we can integrate to a point.

$$w(\theta_o) = -\frac{\Gamma_o}{2\pi b \cos(\Lambda)} \left[\pi - \sin(\Lambda) \left(\int_0^{\theta_o} \frac{\cos(\theta)d\theta}{(\cos(\theta) - \cos(\theta_o))} - \int_{\theta_o}^\pi \frac{\cos(\theta)d\theta}{(\cos(\theta) - \cos(\theta_o))} \right) \right] \quad (20)$$



Unfortunately, I have not been able to find a solution for the final integration yet. Turns out this integral (even for the simple case of $\Lambda = 0$) is very difficult to calculate. A proof of equation 21 is presented in appendix E of [13]. As a result, I will just use numerical integration to find the downwash. It is important to mention that even numerical integration of this equation is not straightforward. Now imagine an oblique wing with an elliptic lift distribution of $\Gamma = \Gamma_o \sin(\theta)$ in which $\Gamma_o = 2\pi b$. The distribution of downwash along the span of an elliptic oblique wing at different angles of sweep of 0, 30, 45, and 60 degrees is presented in figure 27.

As seen in figure 27, we have mostly favorable induced velocity on the right half span for non zero oblique. On the other hand, downwash on the left half span is more severe than the case with zero oblique angle. increasing the oblique angle, results in larger changes in downwash velocity. Interesting to note that downwash changes sign on the right half of the wing.

$$\int_0^\pi \frac{\cos(n\theta)d\theta}{\cos(\theta) - \cos(\theta_o)} = \pi \frac{\sin(n\theta_o)}{\sin(\theta_o)} \quad (21)$$

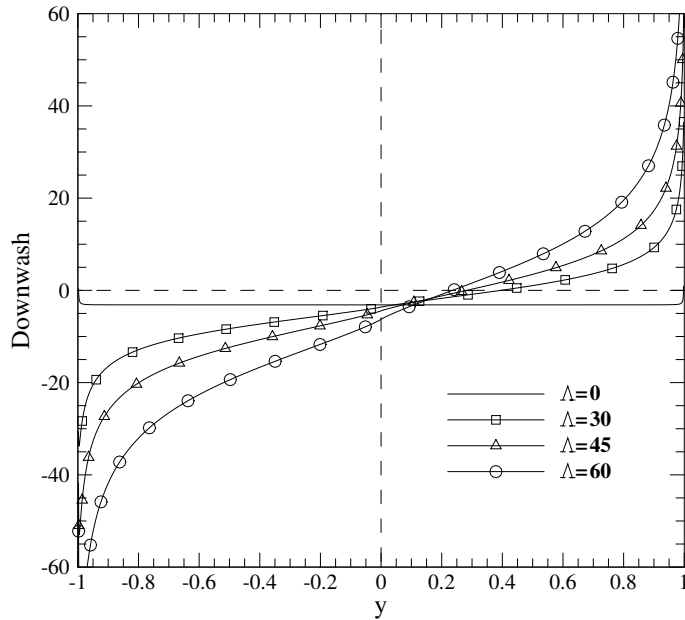


Figure 27: Downwash distribution along the span of an elliptic oblique wing.

Total lift of an oblique wing with elliptic lift distribution can be calculated using the following procedure.

$$L = \rho_\infty U_\infty \cos(\Lambda) \Gamma = \rho_\infty U_\infty \cos(\Lambda) \Gamma_o \int_0^\pi \sin^2(\theta) d\theta = \rho_\infty U_\infty \cos(\Lambda) \Gamma_o \frac{b}{4} \pi \quad (22)$$

Assuming an elliptic lift distribution we have the following.

$$L(\theta) = L_o \sin(\theta) \quad (23)$$

$$L_o = \rho_\infty U_\infty \cos(\Lambda) \Gamma_o \quad (24)$$

$$D_i(\theta) = L \sin(\alpha_i) = \rho_\infty U_\infty \cos(\Lambda) \Gamma_o \sin(\theta) \sin\left(\frac{-w(\theta)}{U_\infty}\right) \quad (25)$$

Assume $\Gamma_o = 2\pi b$ and $U_\infty = 300$ and plot $\frac{D_i(\theta)}{\rho_\infty U_\infty \Gamma_o}$ as in figure 28. This figure shows that for non zero oblique angle on the outer section of the right half span, we are getting induced drag in the direction of movement. Integrating these results which are presented in table 3, shows that the total induced drag decreases with increasing oblique angle :) The same test is carried out at a free stream velocity of at $U_\infty = 100$ and the results are presented in figure 29 and table 4. Again, at higher angles of oblique, the induced drag is reduced. An important thing to note in figures 3 and 4 is that the induced drag is constant at the center of span with changing Λ .

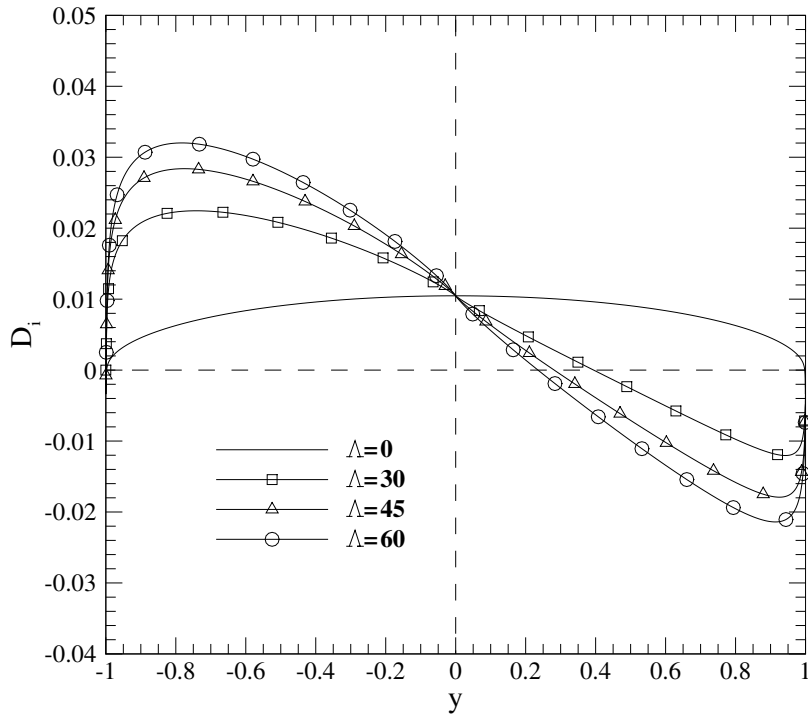


Figure 28: Nondimensionalized induced drag distribution along the span of an elliptic oblique wing at $U_\infty = 300$.

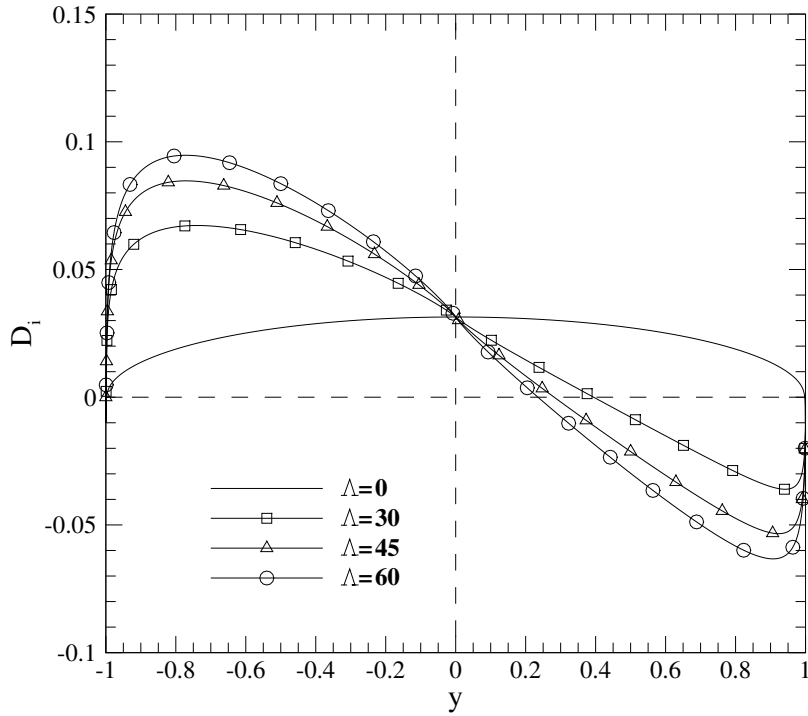


Figure 29: Nondimensionalized induced drag distribution along the span of an elliptic oblique wing at $U_\infty = 100$.

Table 3: Total nondimensionalized induced drag vs. oblique angle of sweep at $U_\infty = 300$.

Λ [degrees]	Total induced drag
0	0.0164236
30	0.0164083
45	0.0163848
60	0.0163361

Table 4: Total nondimensionalized induced drag vs. oblique angle of sweep at $U_\infty = 100$.

Λ [degrees]	Total induced drag
0	0.049264
30	0.049140
45	0.048928
60	0.048419

Such analysis on oblique wings are not new and there are a few previous articles focusing on this matter. Cheng in 1978 [14], extended Prandtl's approach to planar wings including

curved and swept centerlines. Further in 1980 [15], Cheng presented a transonic flow theory of thin, oblique wing of high aspect ratio, which permitted a delineation of the influence of wing sweep, the centerline curvature, and other three-dimensional effects on the nonlinear mixed flow in the framework of small disturbance theory. They carried out upwash corrections which includes the influence of both the near and far wakes, as well as the local curvature of the centerline.

5 Far Field Analysis and the Trefftz Plane

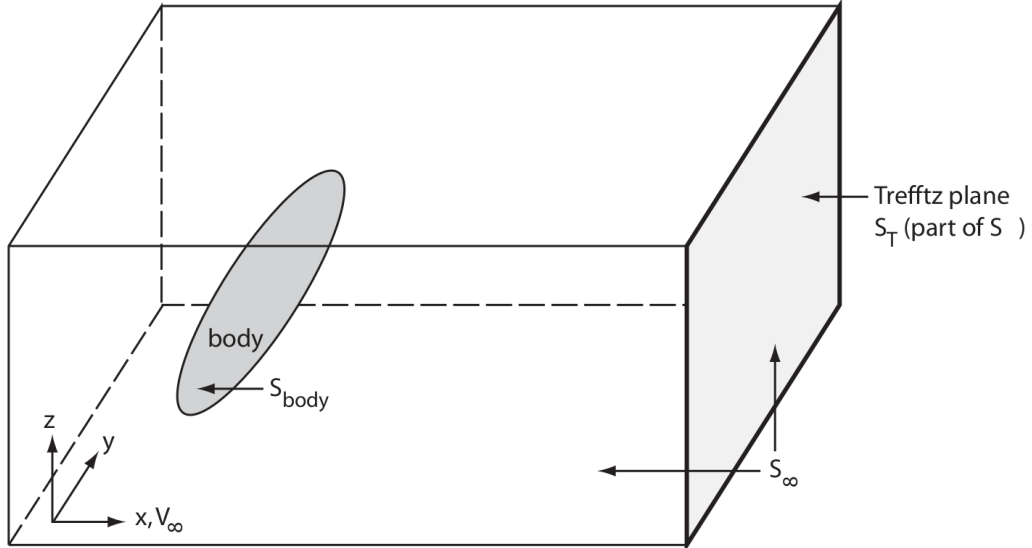


Figure 30: control volume around a finite wing.

Consider an inviscid, incompressible potential flow around a wing and define a control volume surrounding the body as presented in figure 30. Upstream velocity is U_∞ and in x direction which means drag is in x direction as well. We can utilize the momentum integral in x direction to find the drag (induced drag in this case).

$$\iint_{S_{\text{body}}+S_\infty} \rho \vec{V} \cdot \vec{n} dS = - \iint_{S_{\text{body}}+S_\infty} P \vec{n} dS \quad (26)$$

On the body we have $\vec{V} \cdot \vec{n} = 0$.

$$\iint_{S_\infty} \rho \vec{V} \cdot \vec{n} dS = - \iint_{S_{\text{body}}+S_\infty} P \vec{n} dS \quad (27)$$

On the body we also have $-\iint_{S_{\text{body}}} P \vec{n} dS$ (force of body acting on the fluid). The opposite of this force is acting on the body (from fluid) and has three components, drag in x

direction, lift in z direction, and side force in y direction.

$$D\hat{i} + Y\hat{j} + L\hat{k} = \iint_{S_{\text{body}}} P\vec{n}dS \quad (28)$$

As a result:

$$D\hat{i} + Y\hat{j} + L\hat{k} = - \iint_{S_{\infty}} \rho \vec{V} \cdot \vec{n} dS - \iint_{S_{\infty}} P \vec{n} dS \quad (29)$$

The drag component can be extracted as follows.

$$D = - \iint_{S_{\infty}} \rho u \vec{V} \cdot \vec{n} dS - \iint_{S_{\infty}} P \vec{n} \cdot \vec{i} dS \quad (30)$$

Now we can apply Bernoulli equation to eliminate the pressure.

$$P = P_{\infty} + \frac{1}{2}\rho U_{\infty}^2 - \frac{1}{2}\rho(u^2 + v^2 + w^2) \quad (31)$$

$$D = - \iint_{S_{\infty}} \rho u \vec{V} \cdot \vec{n} dS - \iint_{S_{\infty}} \left[P_{\infty} + \frac{1}{2}\rho U_{\infty}^2 - \frac{1}{2}\rho(u^2 + v^2 + w^2) \right] \vec{n} \cdot \vec{i} dS \quad (32)$$

We know that $\iint_{S_{\infty}} \left[P_{\infty} + \frac{1}{2}\rho U_{\infty}^2 \right] \vec{n} \cdot \vec{i} dS = 0$.

$$D = - \iint_{S_{\infty}} \rho u \vec{V} \cdot \vec{n} dS + \iint_{S_{\infty}} \frac{1}{2}\rho(u^2 + v^2 + w^2) \vec{n} \cdot \vec{i} dS \quad (33)$$

Now we can rewrite the free stream velocity into an integral part and perturbation.

$$\begin{cases} u = U_{\infty} + \hat{u} \\ v = 0 + \hat{v} \\ w = 0 + \hat{w} \end{cases} \quad (34)$$

In which \hat{u} , \hat{v} , and \hat{w} are perturbation velocities (not necessarily small). Let's rewrite the drag force with these new velocities.

$$D = -\rho \iint_{S_{\infty}} (U_{\infty} + \hat{u}) \vec{V} \cdot \vec{n} dS + \frac{1}{2}\rho \iint_{S_{\infty}} (U_{\infty}^2 + 2U_{\infty}\hat{u} + \hat{u}^2 + \hat{v}^2 + \hat{w}^2) \vec{n} \cdot \vec{i} dS \quad (35)$$

Again, we know that $\rho \iint_{S_{\infty}} U_{\infty} \vec{V} \cdot \vec{n} dS = 0$ and $\frac{1}{2}\rho \iint_{S_{\infty}} U_{\infty}^2 \vec{n} \cdot \vec{i} dS = 0$.

$$D = -\rho \iint_{S_{\infty}} \hat{u} \vec{V} \cdot \vec{n} dS + \frac{1}{2}\rho \iint_{S_{\infty}} (2U_{\infty}\hat{u} + \hat{u}^2 + \hat{v}^2 + \hat{w}^2) \vec{n} \cdot \vec{i} dS \quad (36)$$



Perturbation velocities on all control volume boundaries far away from the wing are zero except for the downstream plane (Treffitz plane S_T).

$$D = -\rho \iint_{S_T} \hat{u} \vec{V} \cdot \vec{n} dS + \frac{1}{2} \rho \iint_{S_T} (2U_\infty \hat{u} + \hat{u}^2 + \hat{v}^2 + \hat{w}^2) \vec{n} \cdot \vec{i} dS \quad (37)$$

$$D = -\rho \iint_{S_T} \hat{u} (U_\infty + \hat{u}) dS + \frac{1}{2} \rho \iint_{S_T} (\hat{u}^2 + \hat{v}^2 + \hat{w}^2) dS + \rho U_\infty \iint_{S_T} \hat{u} dS \quad (38)$$

Eliminate zero terms.

$$D = -\rho \iint_{S_T} \hat{u} \hat{u} dS + \frac{1}{2} \rho \iint_{S_T} (\hat{u}^2 + \hat{v}^2 + \hat{w}^2) dS \quad (39)$$

$$D = \frac{1}{2} \rho \iint_{S_T} (-\hat{u}^2 + \hat{v}^2 + \hat{w}^2) dS \quad (40)$$

As a final note, we know that trailing vortices far downstream are in x direction which means that $\hat{u} = 0$ on Trefftz plane.

$$D = \frac{1}{2} \rho \iint_{S_T} (\hat{v}^2 + \hat{w}^2) dS \quad (41)$$

Equation 41 shows that the induced drag of a finite wing is in fact the kinetic energy transferred into the cross flow (i.e. the trailing vortices).

using Gauss's theorem, induced drag can be expressed as a line integral over the wake itself.

$$D = -\frac{1}{2} \rho \oint_{\text{wake}} \Gamma V_n dl \quad (42)$$

This simplifies the calculation of drag. V_n is the downwash at the wake far downstream of the wing. As a result, if the wake of any finite wing (including swept and oblique ones) is known we can calculate the induced drag.

5.1 Nonplanar Wakes

All of the comments above apply to nonplanar wings as well as to simple planar ones. But we must be careful about the assumed wake shape when evaluating forces in the far field. The integrals above actually give the force on the wing and wake combination. Of course, in reality, there is no force on the wake sheet, but if we assume a shape a priori, it is not likely to be a force-free wake. However, since forces act in a direction perpendicular to the vortex, extending wakes streamwise always yields a drag free wake and nearly correct answers for drag using far field methods.

5.2 Munk's Stagger Theorem

The result that the drag of a lifting system depends only on the distribution of circulation shed into the wake leads to some very useful results in classical aerodynamics. Perhaps the most useful of these is called Munk's stagger theorem [16]. It states that: *The total*

induced drag of a system of lifting surfaces is not changed when the elements are moved in the streamwise direction. The theorem applies when the distribution of circulation on the surfaces is held constant by adjusting the surface incidences as the longitudinal position is varied. This implies that the drag of an elliptically loaded swept wing (at the same span) is the same as that of an unswept wing. It also is very useful in the study of canard airplanes for which the canard downwash on the wing is quite complicated. Moving the canard very far behind the wing does not change the drag, but makes its computation much easier. One may use the stagger theorem to prove several other useful results. One of these is the mutual induced drag theorem [17] which states that: *The interference drag caused by the downwash of one wing on another is equal to that produced by the second wing on the first, when the surfaces are unstaggered (at the same streamwise location).* These results are especially useful in analyzing multiple lifting surfaces.

6 Conclusion

The present study tried to shine an oblique light on the drag reduction mechanisms of oblique wings. We used XFLR5 and lifting line analysis to characterize the phenomenon in action. As a benchmark, we looked at NASA AD-1 (Ames-Dryden-1) aircraft which utilized a wing that could be pivoted obliquely from zero to 60 degrees during flight. R.T. Jones of NASA Ames Research Center has conducted some of the earliest theoretical studies on this subject, beginning in the 1950s. Further, there has been a number of test flights to prove the feasibility and performance of oblique wings. We presented a historical review of oblique wing airplanes and other oblique wing studies. Then XFLR5 software was utilized to analyze the characteristics and performance of NASA AD-1 wing at zero sweep. I also utilized lifting line theory to analyze the effect of oblique angle on the induced drag. Our lifting line analysis showed a reduction in induced drag with increasing oblique angle. Unfortunately, I don't have enough time to study the effects of flow compressibility on the performance of oblique wings. At transonic and supersonic flights, wave drag is the dominant component of total drag. A significant advantage of oblique wing arrangements for supersonic flight is that they distribute the lift over about twice the wing length compared to a conventional, symmetrically swept wing. This reduces lift dependent wave drag by a factor of 4 and volume dependent wave drag by a factor of 16.



References

- [1] A. Bolonkin and G. B. Gilyard, “Estimated benefits of variable-geometry wing camber control for transport aircraft,” 1999.
- [2] J. R. Hansen, *Engineer in Charge: A History of the Langley Aeronautical Laboratory, 1917-1958*, vol. 4305. Scientific and Technical Information Office, National Aeronautics and Space Administration, 1987.
- [3] T. Gregory, “Oblique wing ready for research aircraft,” 1985.
- [4] R. T. Jones, “Theoretical determination of the minimum drag of airfoils at supersonic speeds,” *Journal of the Aeronautical Sciences*, vol. 19, no. 12, pp. 813–822, 1952.
- [5] M. Alam and K. Narenathreyas, “Oblique wing: Future generation transonic aircraft,” *International Journal of Aerospace and Mechanical Engineering*, vol. 8, no. 5, pp. 888–891, 2014.
- [6] R. Jones, “Dual-fuselage aircraft having yawable wing and horizontal stabilizer,” June 5 1973. US Patent 3,737,121.
- [7] G. Lee, “Slewed wing supersonics,” *The Aeroplane*, vol. 100, pp. 240–241, 1961.
- [8] S. Morris and B. Tigner, “Flight tests of an oblique flying wing small scale demonstrator,” in *Guidance, Navigation, and Control Conference*, p. 3327, 1995.
- [9] W. G. Vincenti, “Robert t. jones, one of a kind,” *Annual Review of Fluid Mechanics*, vol. 37, no. 1, pp. 1–21, 2005.
- [10] R. T. Jones, “Wing plan forms for high-speed flight,” 1946.
- [11] B. Larrimer, *Thinking Obliquely: Robert T. Jones, the Oblique Wing, NASA’s AD-1 Demonstrator, and Its Legacy*. NASA aeronautics book series, National Aeronautics and Space Administration, Aeronautics Research Mission Directorate, 2013.
- [12] J. Anderson, *Fundamentals of Aerodynamics*. McGraw-Hill Education, 2016.
- [13] K. Karamcheti, *Principles of Ideal-fluid Aerodynamics*. R. E. Krieger Publishing Company, 1980.
- [14] H. Cheng, “Lifting-line theory of oblique wings,” *AIAA Journal*, vol. 16, no. 11, pp. 1211–1213, 1978.
- [15] H. Cheng and S. Meng, “The oblique wing as a lifting-line problem in transonic flow,” *Journal of Fluid Mechanics*, vol. 97, no. 3, pp. 531–556, 1980.
- [16] E. Larabee, “Trim drag in the light of munk’s stagger theorem,” 1975.
- [17] L. Demasi, G. Monegato, and R. Cavallaro, “Minimum induced drag theorems for multwing systems,” *AIAA Journal*, pp. 3266–3287, 2017.